



Article

Microscopic Analysis of Natural Fracture Properties in Organic-Rich Continental Shale Oil Reservoirs: A Case Study from the Lower Jurassic in the Sichuan Basin, China

Xuefeng Bai ^{1,2}, Saipeng Huang ^{3,4,*} , Xiandong Wang ^{5,6}, Zhiguo Wang ^{5,6}, Youzhi Wang ^{5,6}, Weiqi Ma ^{5,6}, Yanping Zhu ^{5,6}, Mengdi Sun ³, Bo Liu ³, Xiaofei Fu ³, Lijuan Cheng ³ , Likai Cui ³ and Yudong Hou ⁷

- ¹ School of Geoscience, China University of Petroleum, Qingdao 266580, China
 - ² Exploration Department, PetroChina Daqing Oilfield Company Limited, Daqing 163000, China
 - ³ Key Laboratory of Continental Shale Hydrocarbon Accumulation and Efficient Development, Ministry of Education, Northeast Petroleum University, Daqing 163318, China
 - ⁴ Department de Mineralogia, Petrologia i Geologia Aplicada, Facultat de Ciències de la Terra, Universitat de Barcelona (UB), c/Martí i Franquès s/n, 08028 Barcelona, Spain
 - ⁵ Exploration and Development Research Institute, PetroChina Daqing Oilfield Company Limited, Daqing 163712, China
 - ⁶ Key Laboratory of Continental Shale Oil of Heilongjiang Province, Daqing 163318, China
 - ⁷ College of Resources and Safety Engineering, Chongqing University, Chongqing 400030, China
- * Correspondence: huangspcugb@hotmail.com

Abstract: Natural fractures are of paramount importance in storing carbon in shale oil reservoirs, where ultra-low porosity and permeability necessitate their essentiality for enhanced oil recovery. Therefore, comprehensively clarifying the characteristics of natural fractures in shale oil reservoirs is imperative. This paper focuses on investigating the microscopic features of natural fractures in organic-rich continental shale oil reservoirs that are commonly found in the Lower Jurassic strata of the Sichuan Basin, employing them as a representative example. Multiple methods were utilized, including mechanical testing, Kaiser testing, multi-scale CT scanning (at 2 mm, 25 mm, and 100 mm scales), and a numerical simulation of fluid seepage in fracture models. The results revealed that the in situ stress of the target seam displays the characteristic of $\sigma_H > \sigma_v > \sigma_h$, with σ_v and σ_h being particularly similar. The relatively high lateral stress coefficient (ranging from 1.020 to 1.037) indicates that the horizontal stresses are higher than the average level. Although the 2 mm CT scan provides a more detailed view of fractures and connected pores, it primarily exhibited more pore information due to the high resolution, which may not fully unveil additional information about the fractures. Thus, the 25 mm shale core is a better option for studying natural fractures. The tortuosity of the different fractures indicated that the morphology of larger fractures is more likely to remain stable, while small-scale fractures tend to exhibit diverse shapes. The simulations demonstrated that the stress sensitivity of fracture permeability is approximately comparable across different fracture scales. Therefore, our research can enhance the understanding of the properties of natural fractures, facilitate predicting favorable areas for shale oil exploration, and aid in evaluating the carbon storage potential of shale oil reservoirs.

Keywords: Sichuan Basin; Lower Jurassic; shale oil reservoir; natural fracture; CT scanning



Citation: Bai, X.; Huang, S.; Wang, X.; Wang, Z.; Wang, Y.; Ma, W.; Zhu, Y.; Sun, M.; Liu, B.; Fu, X.; et al. Microscopic Analysis of Natural Fracture Properties in Organic-Rich Continental Shale Oil Reservoirs: A Case Study from the Lower Jurassic in the Sichuan Basin, China. *J. Mar. Sci. Eng.* **2023**, *11*, 1036. <https://doi.org/10.3390/jmse11051036>

Academic Editor: George Kontakiotis

Received: 24 April 2023

Revised: 10 May 2023

Accepted: 10 May 2023

Published: 12 May 2023



Copyright: © 2023 by the authors. Licensee MDPI, Basel, Switzerland. This article is an open access article distributed under the terms and conditions of the Creative Commons Attribution (CC BY) license (<https://creativecommons.org/licenses/by/4.0/>).

1. Introduction

Shale oil is one of the most important unconventional resources [1–5], attracting global attention in recent years [6–12]. The use of hydraulic fracturing technology has made it possible to extract oil and gas from previously uneconomical shale formations [13,14], leading to a shale oil production boom, particularly in the United States and Russia [15–17]. As an alternative to conventional energy, shale oil is leading a new energy revolution to address China's energy shortage [18]. Recent research has shown that shale oil also

has excellent potential in the Qingshankou Formation (Fm) in the Songliao Basin [19] and the Lianggaoshan Fm and Ziliujing Fms in the Sichuan Basin [20]. Notwithstanding the abundant resources of shale oil, its effective exploitation has been hampered by the extremely low porosity and permeability of the reservoirs [21,22]. As such, the recovery of shale oil remains a pressing research focus.

Natural fractures are the primary channels for oil and gas seepage, making them essential for enhanced recovery [23–26]. In addition, natural fractures in reservoirs are crucial for creating a low-carbon environment, as they serve as significant storage spaces for carbon storage [27–32]. Consequently, many scholars have conducted research on shale natural fractures [21,33–36] and the multi-scale dimensional evaluation of natural fractures in shale has been a hot topic [22,37,38]. Information about natural fractures, such as fracture density, filler, orientation, width, and length, can be obtained from shale outcrops [39] and the natural fracture orientation can serve as a vital indicator of the present-day stress field [40]. Additionally, full-diameter shale drill cores can be used to study natural fractures, and macroscopic fractures can be described by observing fresh, unweathered shale cores [22]. Moreover, the Formation MicroScanner Image (FMI) data of formation resistivity can also identify natural fractures [41], though the accuracy of microfracture observation is insufficient. Further research on fracture observation through scanning electron microscope photographs has also been conducted [42], although thin sections may alter the original state of the fracture.

In recent years, there has been an increasing demand for a more precise observation and description of in situ natural fractures. Non-destructive techniques such as radiation X-ray computed tomography (CT) scanning have become a common means of studying in situ fractures and microscopic pores [43–46]. Gou et al. (2019) [45] used nano-CT and micro-CT to finely study the pore-fracture structure of shales, but the study primarily focused on the pore system. However, numerous advanced representation techniques have been utilized to thoroughly investigate the connectivity of shale pores, as extensively documented in studies by Sun et al. (2016, 2020) [47,48]. On the other hand, the shale fracture shape can be well revealed by using micron-CT [49] and the fracture length, width, connection forms, and tortuosity as well. Furthermore, CT scanning can also be used to monitor fracture propagation in real-time [44]. Additionally, numerical modeling based on the geometries of reservoir rocks can be established using CT scanning, and further coupling studies can be conducted using COMSOL [50].

While CT scanning is a widely used technique for studying natural fractures in shale, there has been limited research on the comparative characterization of these fractures using different core sizes. The investigation of corresponding natural fracture characteristics across different scales remains largely understudied. Therefore, this study investigates the characteristics of natural fractures in continental shale oil reservoirs of the Lower Jurassic in the Sichuan Basin at the microscopic scale using multi-scale cores. To achieve this goal, various methods, such as mechanical testing, Kaiser testing, and multi-scale CT scanning (at 2 mm, 25 mm, and 100 mm scales), were employed. In addition, numerical simulations of the fluid seepage in fracture models were conducted to study the fluid seepage characteristics in fractures at different scales. Thus, this paper presents a novel and comprehensive approach, particularly, by combining the CT scanning technique with the finite element method (FEM) to enable the microscopic observation of fractures and the numerical simulation of fluid flow in fluid–solid coupling within the fracture. This approach allows for an investigation into the characterization of microscopic fractures in shale oil reservoirs. Therefore, the results of this study can contribute significantly to a better understanding of the properties of natural fractures and aid in predicting favorable areas for shale oil exploration.

2. Geological Setting

The Sichuan Basin is a significant resource-based basin in China, known for its abundant shale oil and gas reserves [22]. This basin is a first-order tectonic unit of the Yangzi

Platform that formed during the Indo–Chinese period and was later folded and deformed by the Himalayan movement, resulting in its current tectonic condition. Based on its geomorphological features, the Sichuan Basin can be further classified into six zones: the low and gentle tectonic zone in north Sichuan, the low and steep tectonic zone in west Sichuan, the gentle tectonic zone in central Sichuan, the low and folded tectonic zone in southwest Sichuan, the low and steep tectonic zone in south Sichuan, and the high and steep tectonic zone in east Sichuan (Figure 1a).

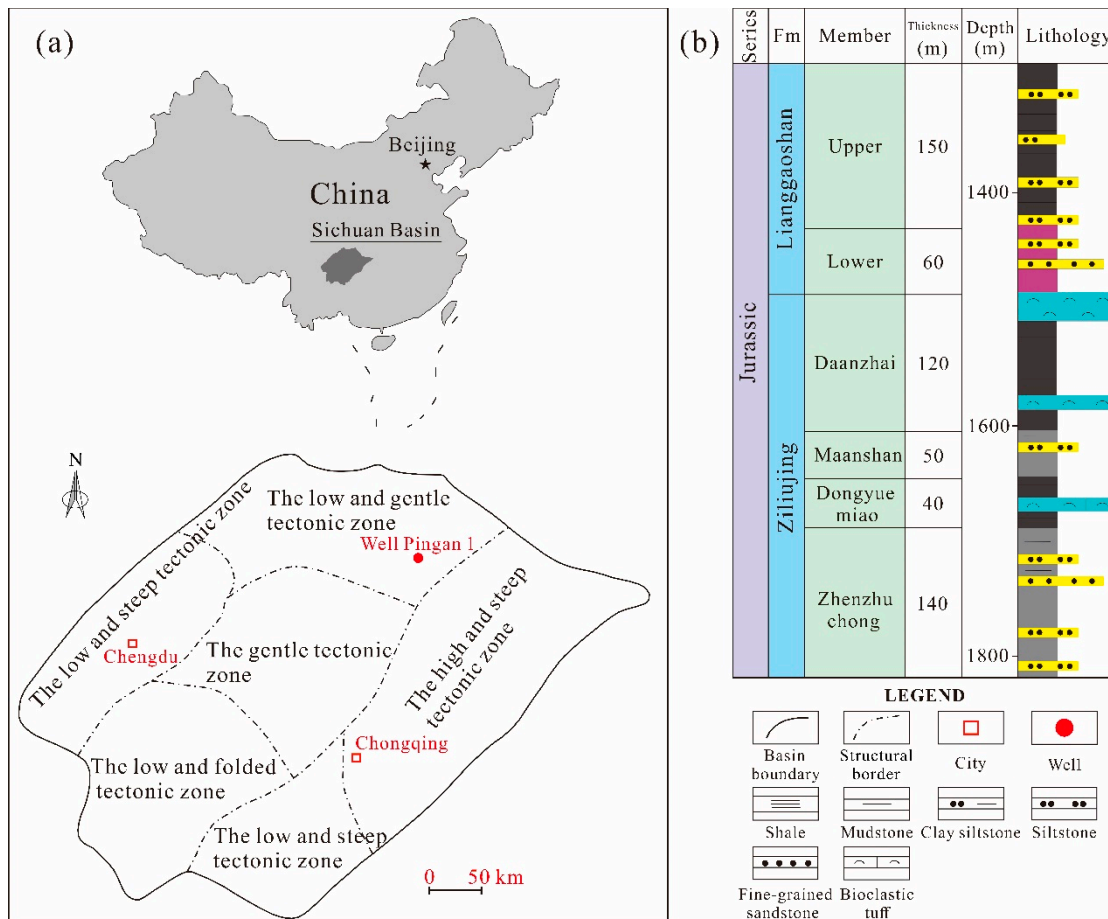


Figure 1. (a) The detail location of the Sichuan Basin, and its structural outline. The star in the figure represents the capital of China, the red square-shaped and circle represent the city and well, respectively; (b) the comprehensive stratigraphic column of the Jurassic, Sichuan Basin. The different colors in (b) indicates the different levels of stratigraphic units, like Series, Fms, and member.

The Jurassic sedimentary assemblage in the Sichuan Basin is primarily composed of clastic rocks interspersed with tuffs, covering an area of approximately $18 \times 10^4 \text{ km}^2$, with thickness varying from 500 to 4500 m. The southern region of the basin presents a relative thinness in comparison to the substantially thicker formations found in the northern basin. The basin’s Jurassic formations are divided from bottom to top into the Ziliujing Formation (ZLJ Fm), the Lianggaoshan Formation (LGS Fm), the Shaximiao Formation (SXM Fm), the Suning Formation (SN Fm), and the Penglaizhen Formation (PLZ Fm) (Figure 1b). While the Lower Jurassic is well-preserved in the Sichuan Basin, the SXM Fm of the Middle Jurassic and other formations have suffered various degrees of denudation and they are relatively well-preserved only in the central Sichuan Basin.

This study collected shale samples from the typical exploration well Pingan 1. The upper section of the LGS Fm in Pingan 1 is further divided into three sublayers: the upper LGS-1, the upper LGS-2, and the upper LGS-3. Among them, the percentage of clayey feldspathic quartz shale in the upper LGS-1 is 54.8%. The average content of clay minerals

is 44.3% and the quartz content is 46.9%, with small amounts of calcite and pyrite. The porosity of the upper LGS-1 ranges from 0.86% to 4.66%, with an average of 2.84%. The TOC (total organic carbon) content ranges from 0.57% to 2.56%, with an average of 1.35%. The shale of the upper LGS has a high content of brittle minerals; in particular, the brittle mineral content of the upper LGS-1 ranges from 40.6% to 74.7%, with an average of 54.8%. As shown in Figure 1a, Pingan 1 is located in the low and gentle tectonic zone, and its shale oil production has reached 112.8 m³/d, a high yield [51]. The shale samples were obtained from Pingan 1 at an average depth of 3011.2 m.

3. Experiments and Methodology

The present study incorporates a combination of experimental tests and numerical simulation methods which consequently provide a comprehensive overview of the principles and techniques employed in CT scanning and FEM numerical simulations.

3.1. The Mechanics of the Shale Oil Reservoir

The development of natural fractures in shale oil reservoirs typically involves two processes: fracture initiation and propagation. Type I fractures (tension cracks), which are the most hazardous among type II (shear cracks) and type III (tension–shear cracks), initiate when the tensile stress exceeds the rock's tensile strength. Additionally, fracture toughness is a crucial parameter that indicates the rock's ability to resist fracture propagation. Thus, both of these mechanical parameters have a significant impact on fracture development.

The Brazilian splitting test is a highly effective method for determining both the tensile strength and fracture toughness of rocks [52,53]. To prepare the specimens for the test, samples are taken from vertical strata and cut into three pieces, which are then standardized to ensure a height-to-diameter ratio of 1. The rock samples are then carefully machined to meet the requirements of the International Society for Rock Mechanics' Recommended Test Specification. The size, mass, and density of the specimens are all carefully documented in Table 1. In addition to evaluating the rock's tensile strength, the Brazilian splitting test also assesses its fracture toughness by introducing pre-fabricated cracks into the specimens. Specifically, three semi-disc specimens are extracted from the vertical strata and manual cracks are created to achieve a height-to-crack length ratio of 0.5, as required by the standard. More detailed specifications of the specimens are provided in Table 2.

Table 1. The specimens used for testing tensile strength.

No.	Length (mm)	Diameter (mm)	Weight (g)	Density (g/cm ³)
1-1	26.02	24.68	32.21	2.59
1-2	23.98	24.02	29.58	2.72
1-3	24.55	25.54	32.54	2.59

Table 2. The specimens used for testing fracture toughness.

No.	Height (mm)	Diameter (mm)	Thickness (mm)	Prefabricated Crack Length (mm)
2-1	38.07	76.07	23.13	19.00
2-2	39.51	75.65	23.34	19.00
2-3	36.62	75.48	23.68	19.00

The test apparatus is a rock multi-field coupling triaxial tester with a maximum axial testing force of 500 KN and a deformation measurement error of less than $\pm 0.5\%$. The apparatus is capable of controlling temperatures ranging from room temperature to 150 °C, with a temperature control accuracy of ± 0.5 °C. To determine the tensile strength, the test was performed after axial compression loading at a rate of 0.001 mm/s until the residual strength value was noticeable. During the fracture toughness assessment, the axial loading rate was controlled at a slower pace of 0.0001 mm/s. The highest axial load and

the displacement of the specimen at the time of failure were recorded and documented. Finally, the specimen was removed, and a displacement–load curve was plotted to depict the specimen’s degradation.

In addition, assessing the present-day in situ stress state can provide insight into the propagation behavior of natural fractures in shale oil reservoirs. The Kaiser effect test, which is an effective experimental method that has been commonly used for determining in situ stress [23,54,55], was carried out to obtain the present-day in situ stress of the Pingan 1 well. The Kaiser effect of rocks can be used to measure the historical maximum stress that the rock has undergone. In general, a uniaxial loading test is performed on rock samples, and the emitted sound signals are detected using an acoustic emission instrument. The stress corresponding to the Kaiser point, which is the abrupt increase in the number of sound emissions observed in the relationship between the emitted sound signals and stress, is considered to be the historical maximum stress that the rock has experienced. Typically, a rock sample is taken vertically from the full-size core and three samples are taken horizontally at an incremental angle of 45°. The Kaiser test was performed on the three group rock cores (a total of 12 specimens) with an average depth of 3011.2 m. After conducting measurements, we were able to determine the in situ stresses of three-layer sections located at depths of 3010.00 m, 3010.60 m, and 3013.00 m.

3.2. The CT Scanning of Multi-Scale Shale Cores

The tests were carried out with a CT scanner apparatus of the GE Phoenix Nanotom S at the Northeast Petroleum University, China. A detailed schematic of the X-ray CT scanning setup is shown in Figure 2. Its maximum resolution is approximately 200 nm, which is sufficiently fine to display the cores’ information. The sample diameter that the CT scanner can hold to test ranges from 1 to 120 mm, which fulfills the test requirements. The advantages of using CT scanning include (1) its ability to provide a comprehensive view of very small feature surfaces from a large amount of image data without destroying the sample and (2) the CT images reflect information on the energy decay of the X-rays as they penetrate the object. The pore structure and the relative density value within the core are positively correlated by the grey scale of the 3D CT images. Therefore, the 3D digital core can make a qualitative analysis and quantitative evaluation of pore throat size, connectivity, and morphology.

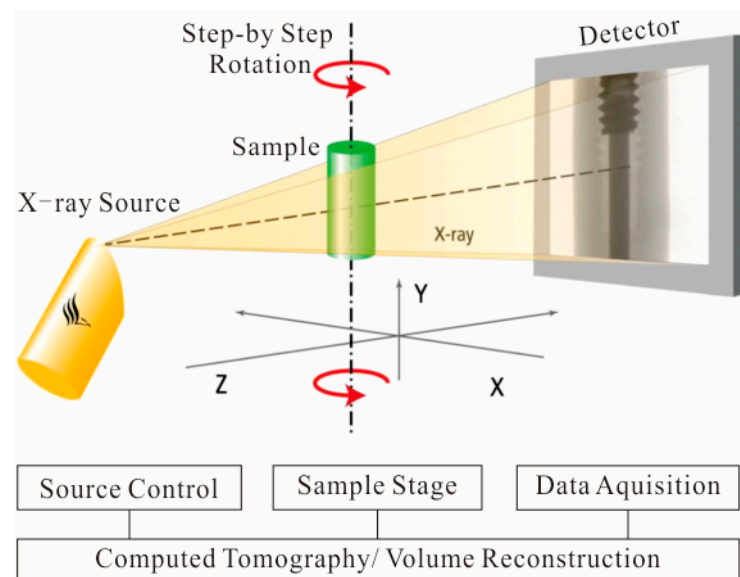


Figure 2. Schematic diagram of the X-ray CT scanning setup. The X-ray source and sample are represented by yellow and green colors, respectively. The coordinate axes show the directions, and red arrows demonstrate the rotation direction during the test.

Compared to experimental analysis methods, such as mercury piezoelectricity and scanning electron microscopy, CT scanning has an advantage in the rapid and non-destructive scanning of rock samples in a wide range and in all directions. The digital cores obtained by CT scanning can be used to study the microscopic pore and fracture characteristics of the reservoir in a more intuitive way, and their application on microscopic pore and fracture structure evaluation is more extensive.

For the purpose of achieving a comparative study on the morphological characteristics of the microfracture at multi-scales, three kinds of core sizes, including 100 mm, 25 mm, and 2 mm, are selected for the scanning test and then analyzed to display the fracture morphology using the program Avizo. The scanning accuracy of the 2 mm core samples ranges from 0.92 to 1.25 μm. Their detailed parameters, including fracture length, width, connection forms, tortuosity, etc., are then displayed and analyzed.

3.3. Natural Fracture Simulation

The use of CT scans can effectively showcase the natural fracture features of shale and enable seepage simulations in typical shale fractures with fluid–solid coupling, allowing for a better understanding of the types of fractures that contribute to the increased seepage capacity of shale reservoirs. To accomplish this, realistic fracture models were created using the CT scans, and seepage simulations were conducted on different natural fracture types. The fluid–solid coupling process was carried out through the use of COMSOL Multiphysics, a simulation software that utilizes various physics interfaces to model fluid–solid coupling processes, such as fluid flow, heat transfer, solid mechanics, and other relevant phenomena. The software uses the FEM to solve the mathematical equations that describe the physical behavior of the system. FEM is a widely used method for modeling fluid–solid interactions [56]. In COMSOL, the fluid–solid coupling is implemented through two physics interfaces: the fluid flow interface and the structural mechanic interface. The fluid flow interface models the behavior of fluids, including velocity, pressure, temperature, and density, while the structural mechanics interface models the behavior of solid materials, including stress, strain, and deformation. The software utilizes boundary conditions to achieve these goals. Additionally, COMSOL allows for non-linear fluid–solid interaction, where the behavior of the fluid and the solid are mutually affected. Overall, COMSOL is a powerful tool for modeling fluid–solid coupling processes, offering a wide range of options for defining the physics, geometry, and boundary conditions of a system.

In this study, we present a fully coupled simulation of the mutual interactions between fluids and solids in coal, implemented using the COMSOL software. The fluid in the channel is assumed to be in a state of fully developed laminar flow, with a constant density and incompressible viscous flow of gas. Thus, the flow of fluid in the channel is described by the incompressible Navier–Stokes equations for the velocity field $u(u, v)$ in the moving spatial coordinate system and pressure p .

$$\rho \frac{\partial u}{\partial t} + \rho((u - u_0) \cdot \nabla)u - \nabla \cdot \left[-pI + \eta(\nabla u + (\nabla u)^T) \right] = F \tag{1}$$

$$-\nabla \cdot u = 0 \tag{2}$$

Here, the I denotes the unit diagonal matrix and F represents the volume force affecting the fluid. Assuming that there is no gravity or other volume force affecting the fluid (i.e., $F = 0$), the velocity of the coordinate system is denoted by $u_0(u_0, v_0)$.

The fluid exerts a force on the structural wall, generated by viscous resistance and fluid pressure, causing the elastic deformation of the coal skeleton, which is compressed under external loading. The outer boundary of the coal sample is fixed, and all boundaries in contact with the fluid domain are subject to the load imposed by the fluid, except for the outer boundary. The formula is given below:

$$F_T = -n \cdot \left(-pI + \eta(\nabla u + (\nabla u)^T) \right) \tag{3}$$

Here, n denotes the normal vector of the boundary. This load represents the sum of pressure and viscous forces.

The pressure and velocity of the fluid and solid domains are transmitted through their common boundaries, and the Arbitrary Lagrangian–Eulerian (ALE) method is used to handle geometric deformation and boundary movement through dynamic meshing [57].

$$v_t(x_0, y_0) = \frac{\partial v}{\partial t} \Big|_{x_0, y_0} \tag{4}$$

$$v_{Time}(X_n, Y_n) = \frac{\partial v}{\partial t} \Big|_{X_n, Y_n} \tag{5}$$

where X and Y are the material frame coordinates and x and y are the coordinates of the spatial frame.

Figure 3 displays the models created from the CT scan data of two different shale core sizes: 100 mm and 25 mm. The models used in the simulations were created using the following process: (1) identifying fractures from scanned sections, as shown in Figure 3a,e, (2) segmenting the data based on specific thresholds, displayed in Figure 3b,f, (3) reconstructing a 3D model structure, as seen in Figure 3c,g, and (4) refining appropriate grids based on the size of the structure, as demonstrated in Figure 3d,h.

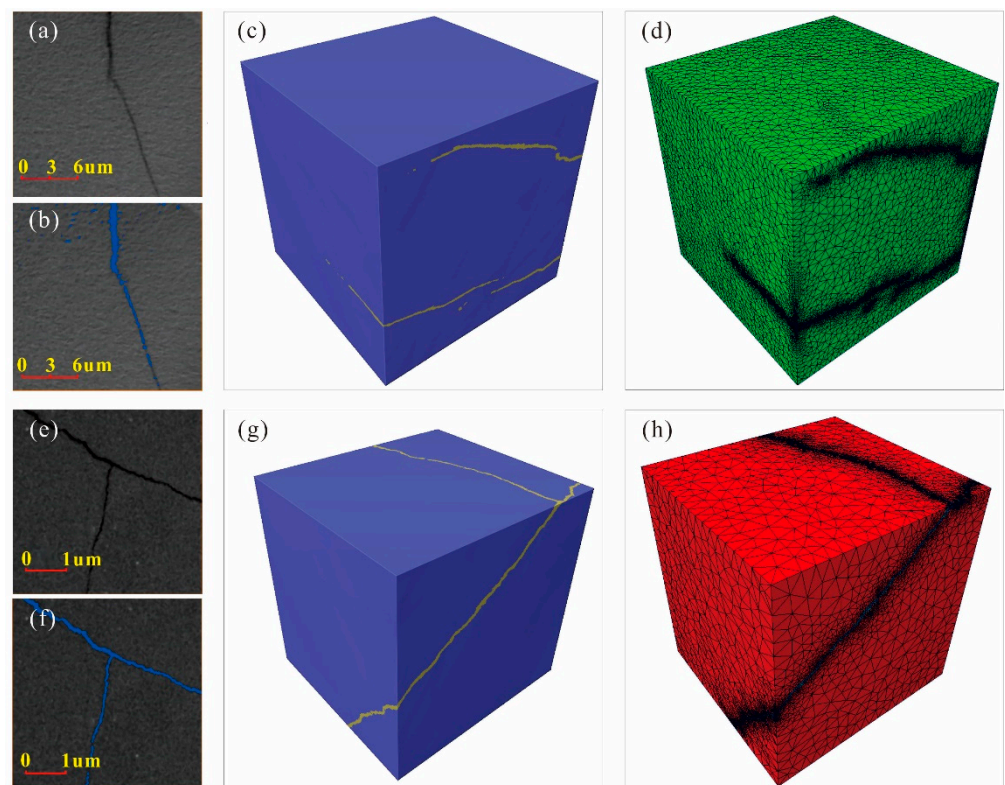


Figure 3. A detailed description of the process for creating models based on the CT scanning data from 100 mm and 25 mm shale cores. The process includes identifying fractures from scanned sections (a,e), segmenting the data based on specific thresholds (b,f), reconstructing a 3D model structure (c,g) displaying with the blue color, and refining appropriate grids based on the size of the structure (d,h), displaying with green and red colors, respectively.

In addition, the models were established using the following parameters: a density of 2.65 g/cm³, a tensile strength of 8 MPa, a compressive strength of 46.67 MPa, a Young’s modulus of 1.33 GPa, and a Poisson’s ratio of 0.21. The model obtained from the 100 mm shale core has a side length of 22,832 μm and a mesh count of 1,342,627, as shown in Figure 3d. In contrast, the model obtained from the 25 mm shale core is much smaller, with

a side length of 5576 μm and a mesh count of 492,140. Both models use tetrahedrons to divide the mesh. Within the framework of the fluid–solid coupling simulation, the fractures present in the models serve as the principal conduits for CH_4 , the gas under investigation, to permeate through the system.

4. Results

4.1. The Shale Oil Reservoir’s Mechanical Data

For the tensile strength test, the shale oil reservoir’s breakdown pressures were recorded as 7.26 kN, 10.50 kN, and 3.30 kN (Figure 4a–c) and the corresponding tensile strengths were 7.20 MPa, 11.60 MPa, and 3.35 MPa. In terms of values, there was a significant variation in the tensile strength of the different specimens, even if they were collected from the same depth. When testing the fracture toughness, the breakdown pressures were recorded as 1.55 kN, 2.14 kN, and 1.66 kN (Figure 4d–f). The fracture toughness of the specimen was calculated using the elastic solution of the Brazilian cleavage test for the collected data. The corresponding fracture toughnesses were $0.26 \text{ MPa}\cdot\text{m}^{1/2}$, $0.36 \text{ MPa}\cdot\text{m}^{1/2}$, and $0.28 \text{ MPa}\cdot\text{m}^{1/2}$. Overall, the magnitude of the tensile strengths and fracture toughness varied a little, however, they exhibited similar mechanical characteristics.

The in situ stress obtained by the Kaiser test is displayed in Table 3. The average in situ stresses were determined for the target reservoirs, with the maximum horizontal stress (σ_H), vertical stress (σ_v), and minimum horizontal stress (σ_h) values being 81.21 MPa, 76.83 MPa, and 76.42 MPa, respectively. The stress gradients of σ_H , σ_v , and σ_h varied from 2.69 to 2.71 MPa/100 m, 2.51 to 2.57 MPa/100 m, and 2.50 to 2.57 MPa/100 m, respectively. Moreover, the lateral stress coefficients ranged from 1.020 to 1.037.

Table 3. Present-day in situ stress of the shale oil reservoir of the Pingan 1 well.

No.	σ_H (MPa)	σ_H Stress Gradient (MPa/100 m)	σ_v (MPa)	σ_v Stress Gradient (MPa/100 m)	σ_h (MPa)	σ_h Stress Gradient (MPa/100 m)
3-1	80.99	2.69	77.29	2.57	76.64	2.55
3-2	81.61	2.71	75.64	2.51	75.31	2.50
3-3	81.03	2.69	77.56	2.57	77.32	2.57

4.2. The Microscopic Dimensions of Natural Shale Fractures

The study utilized CT scans to examine the morphological characteristics of natural fractures across multiple scales, specifically focusing on three different core sizes of 100 mm, 25 mm, and 2 mm. Figure 5 displays the CT scanning result of a full-diameter shale core with a diameter of 100 mm. Figure 5a,b shows grayscale images of two different cross-sections, revealing clearly visible natural fractures, one of which measures approximately 1 mm wide. The cross-sectional slicing of the shale core helps to demonstrate the two-dimensional morphological characteristics of natural fractures; however, it is hard to present their three-dimensional (3D) shape. For example, it is apparent that some of the fractures are continuously distributed in the vertical direction when comparing Figure 5a,b, however, it is obvious that the same fracture shows a different shape in different cross-sections. The CT scanning of the full-diameter core in 3D is shown in Figure 5c,d. Depending on the method of presentation, Figure 5c,d displays the CT scanning’s grayscale image and pseudo-color image, respectively. The 3D morphology of the fractures is effectively visualized, revealing that the fractures exhibit a vertical orientation, as evidenced by the results obtained. However, in the case of full-diameter shale cores, fractures with dimensions below the millimeter range could not be adequately captured owing to the low precision of the scanning technique employed.

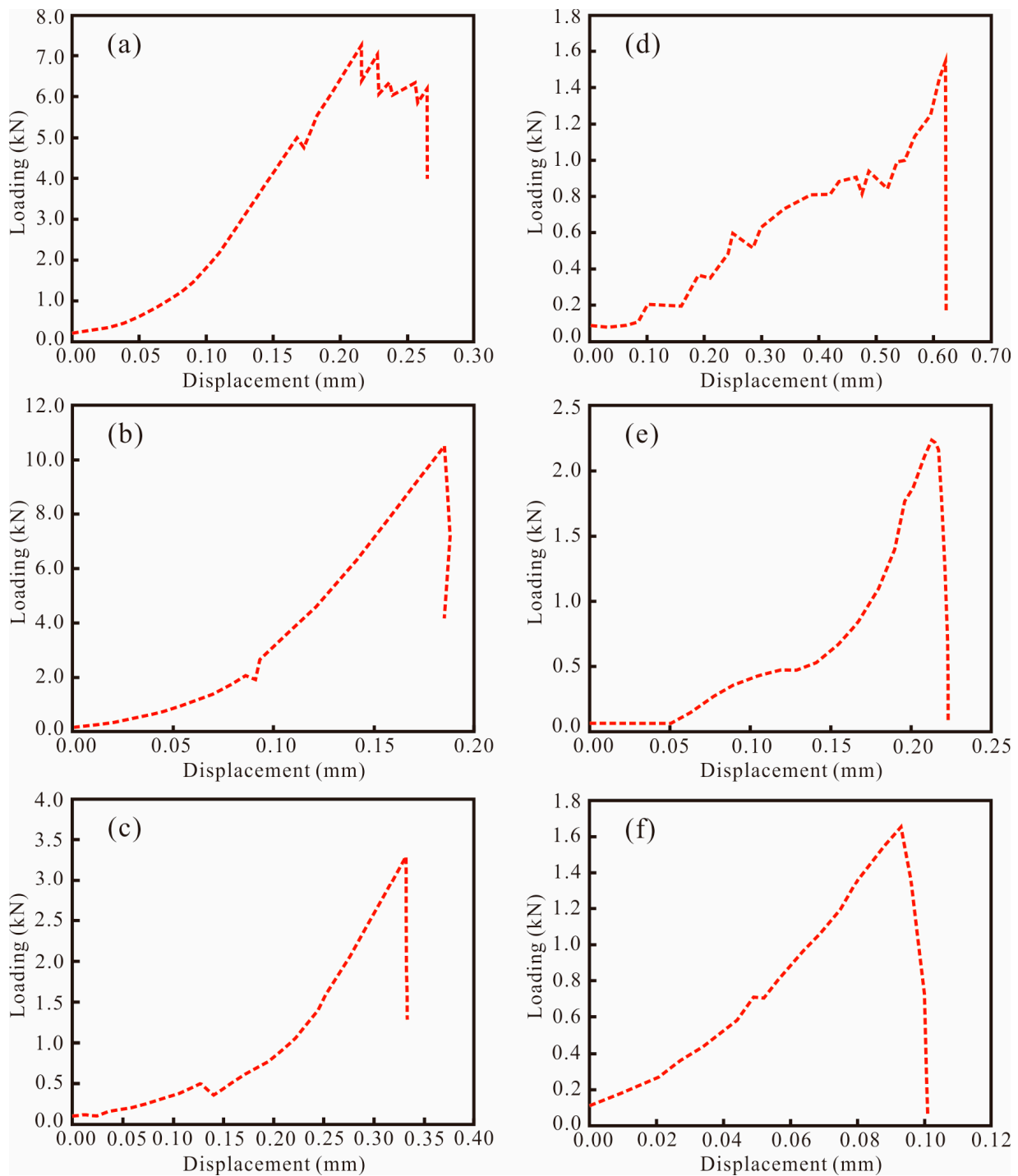


Figure 4. Maximum axial loading and corresponding displacement during tensile strength (a–c) and fracture toughness tests (d–f). The red dot lines show the displacements along with the variation of the loading.

When scanning a 25 mm shale core, reducing the core size results in a significant improvement in scanning accuracy (Figure 6). The deep black line in Figure 6a demonstrates a fracture with a stronger tortuosity. The two longitudinal cross-sections of the core show at least three fractures that are close to parallel to each other (Figure 6b), indicating that they are most probably bedding planes. The different colors in Figure 6c show connecting pores in the vicinity of the fractures. The volume and shape of the bedding planes are presented by the colored plane (Figure 6d). It can be seen that the fracture planes are not continuously

distributed but intermittently. The perspectival modeling of pores and fractures can demonstrate all visible pores and identifiable fractures simultaneously (Figure 6e), though it is worth noting that the pore development between the two fractures is significantly reduced. Moreover, the fractures can be extracted individually to show their detailed information. As shown in Figure 6f, the different colors represent different fracture planes.

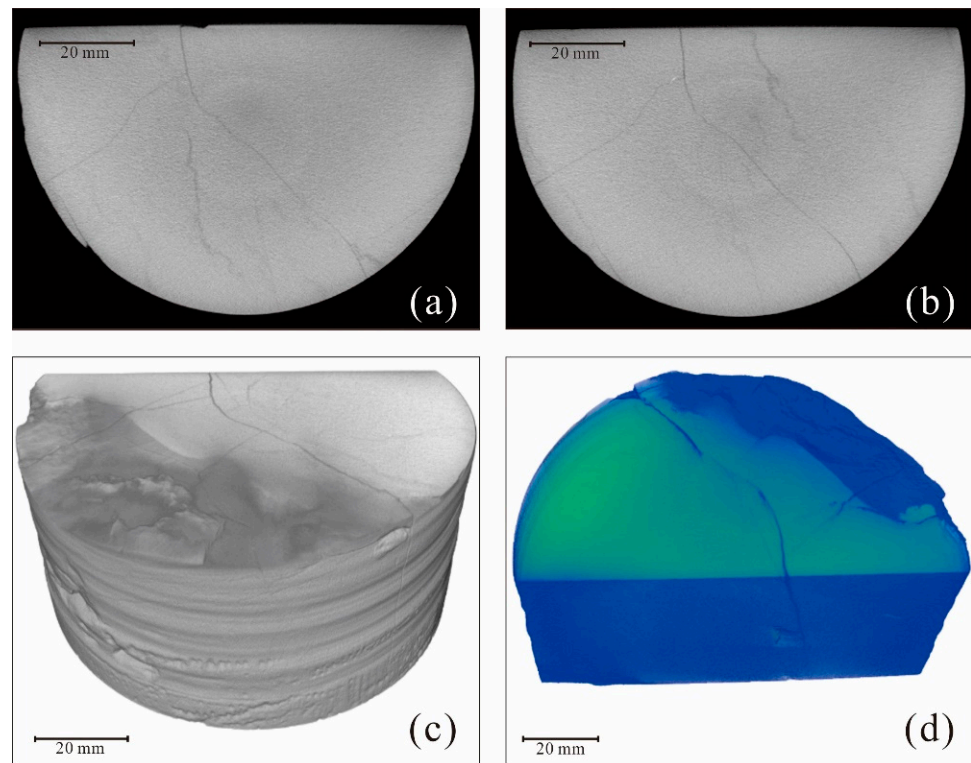


Figure 5. The CT scanning of a 100 mm shale core. (a,b) Display of the grayscale images of two different cross-sections; (c) a 3D representation of the CT scanning's grayscale image; (d) a 3D representation of the CT scanning's pseudo-color image. The color in (d) is pseudo-color which is a form of expression for the interpretation of CT scanning image data.

By reducing the core scale to 2 mm, the scanning accuracy improves to $0.92\ \mu\text{m}$. This level of precision allows fractures and pores in the material to be more clearly visible, as shown in Figure 7. Specifically, Figure 7a displays a cross-section that reveals approximately five fractures, one of which measures around $20\ \mu\text{m}$ in width. Different from the 25 mm core, the fractures shown in the 2 mm core are not bedding planes although they come from the same core. Figure 7b shows the enlarged part of Figure 7a; it indicates that the three fractures trend to propagation in the same direction. Figure 7c,d presents the connectivity fracture model and segmental display of the connectivity in the core, respectively. The displayed fractures are much finer than Figure 6f and more disconnected pores appear around the fractures. Based on the inclination angle of the fractures, they appear to belong to an inclined fracture. The pore–fracture model reveals finer details of the micropores, which are distributed randomly (as shown in Figure 7e). Additionally, the segmented model of the pore–fracture body demonstrates that more interconnected pores are present in wider fractures (as shown in Figure 7f).

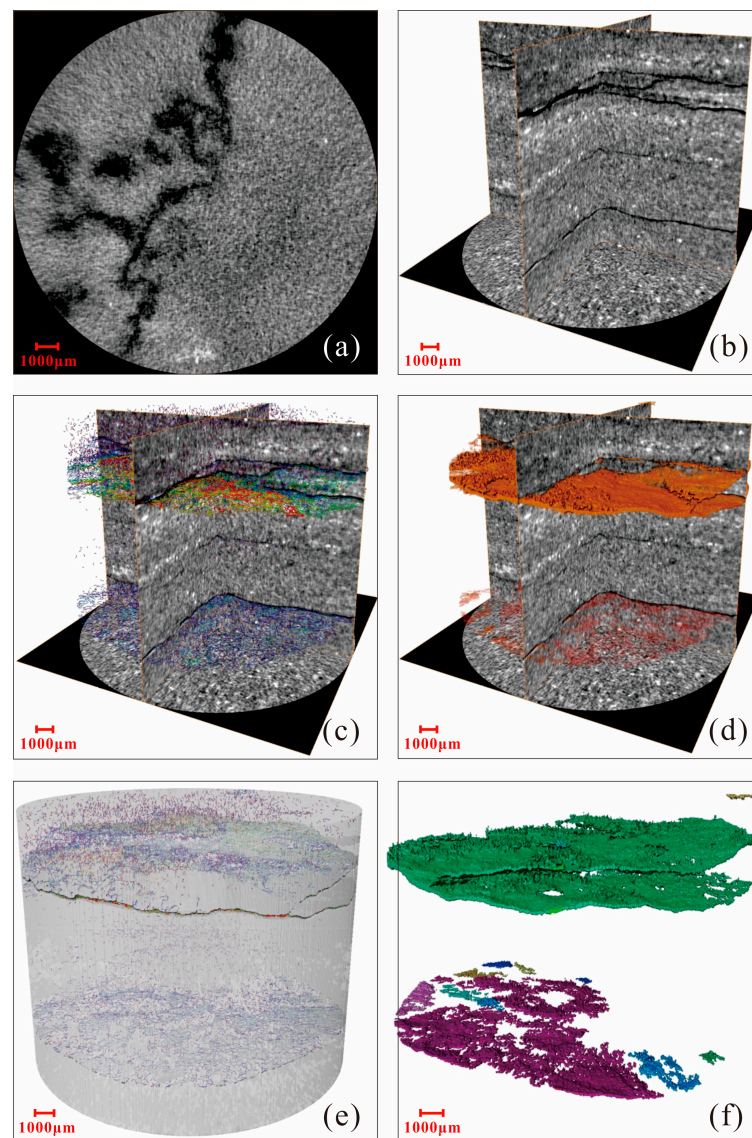


Figure 6. The CT scanning of a 25 mm shale core. (a) Display of one of the cross-sections of the core; (b) the longitudinal cross-section of the core; (c) the longitudinal cross-section of the core showing the pores; (d) the longitudinal cross-section of the core showing the natural fractures; (e) the perspectival modeling of the pores, and (f) the perspectival modeling of the natural fractures. The colorful part in the (c–f) are mainly applied to exhibit the pore–fracture space.

4.3. The Tortuosity Features at Different Shale's Natural Fracture Scales

The tortuosity of the fractures in the 100 mm and 25 mm shale cores were also obtained and analyzed. Figure 8 shows the statistical fractures' tortuosity of four cross-sections of a 25 mm shale core. This CT scan revealed a total of six visible fractures, identified by serial numbers I, II, III, IV, V, and VI. The fractures can be classified into two groups based on their visible length: the long fractures, consisting of numbers I, II, and III, and the short fractures, consisting of numbers IV, V, and VI. Figure 9 shows the statistical fractures' tortuosity of four cross-sections of a 100 mm shale core. As the fractures did not run through the entire full-diameter shale core, only those parts with fractures were selected for display. There are only two fractures visible which are numbered I and II.

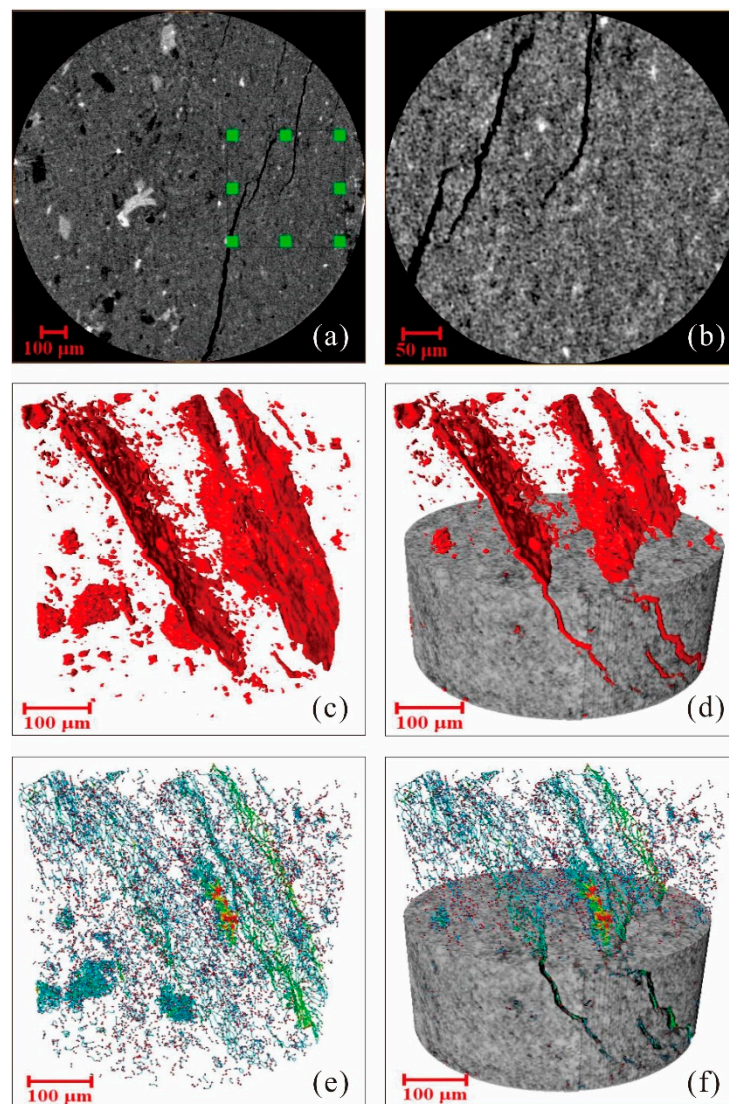


Figure 7. The CT scanning of 2 mm shale core. (a) Display of the cross-sections in the core; (b) an enlarged portion of (a); (c) the red color shows the connectivity model; (d) segmental display of the connectivity in the core; (e) detailed presentation of the pore–fracture model, and (f) the segmented display model of the pore–fracture body. The red color in (c,d) mainly represent the connectivity fracture, while the colorful part in (e,f) mainly show the pore–fracture space.

The fractures' tortuosity is used to describe the fracture roughness in a cross-section, which is calculated by l/L , where l is the real length of the natural fracture and L is the straight-line distance between the two fracture endpoints [22]. In Figure 10, the tortuosity of each fracture in different cross-sections was calculated and compared for a 25 mm shale core, with the resulting range typically falling between 1.00 and 1.06. For the long fractures of I, II, and III, the tortuosity variation ranged from 0.01 to 0.02, while the range increased to 0.03 for the short fractures of IV, V, and VI. Similarly, in a 100 mm shale core, the fractures' tortuosity exhibited a similar changing trend, with values ranging from 1.002 to 1.016 and a range of tortuosity variation between 0.009 and 0.014 (Figure 11).

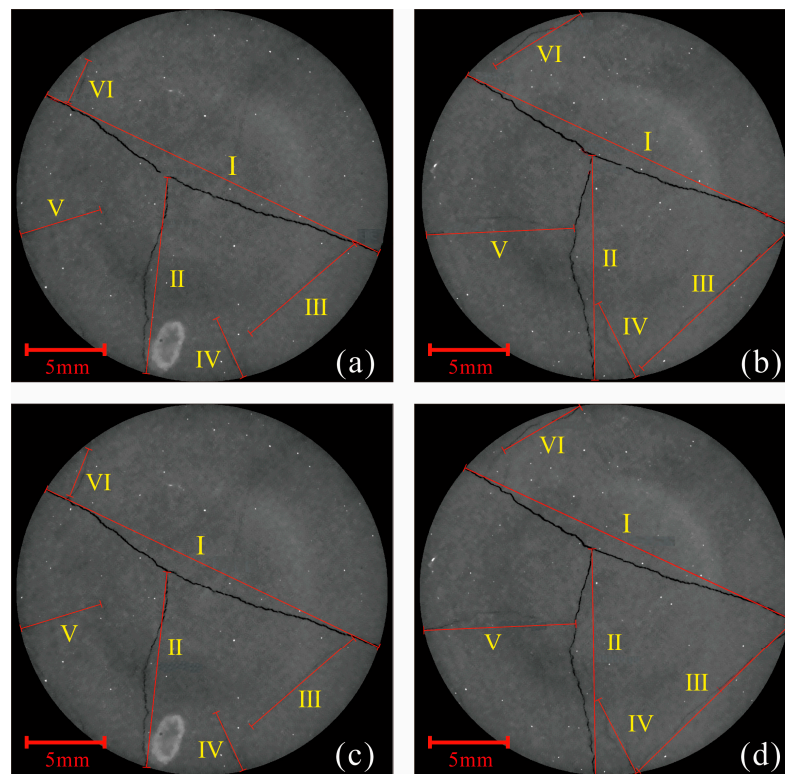


Figure 8. Statistical fractures' tortuosity of four cross-sections of a 25 mm core. The (a–d) corresponding to the four cross-sections of this 25 mm core. Except for the red scale, the red straight lines in the figure show the distance between the ends of the fractures. The yellow roman numbers of I, II, III, IV, V, and VI in the figure are corresponding to the number of the fractures.

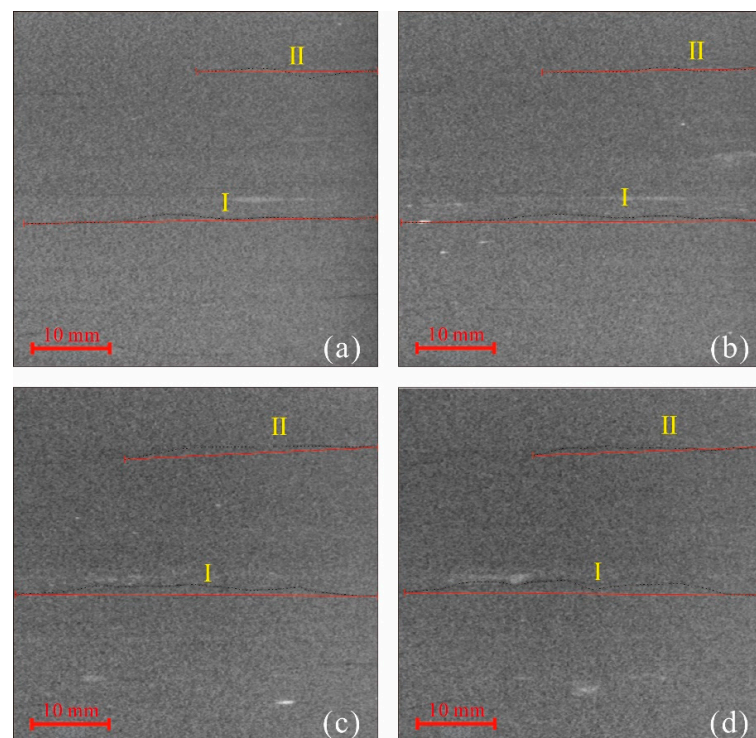


Figure 9. Statistical fractures' tortuosity of four cross-sections of a 100 mm core. The (a–d) corresponding to the four cross-sections of this 100 mm core. Except for the red scale, the red straight lines in the figure display the distance between the ends of the fractures. The yellow roman numbers of I and II in the figure are the number of the fractures.

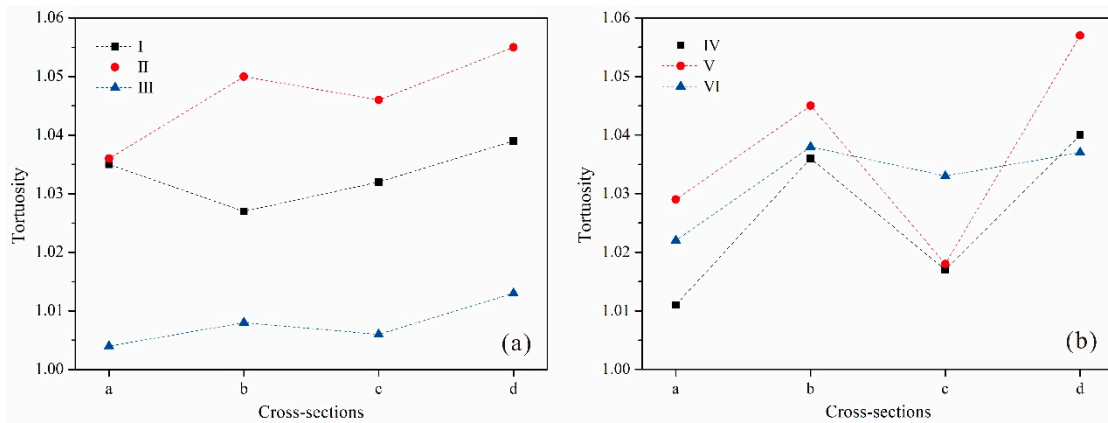


Figure 10. (a) The long fractures’ tortuosity in four cross-sections of a 25 mm core; (b) the short fractures’ tortuosity in four cross-sections of a 25 mm shale core. The (a), (b), (c), and (d) represent the four cross-sections in Figure 8, while the I, II, III, IV, V, and VI in the figure are the corresponding fracture number in Figure 8.

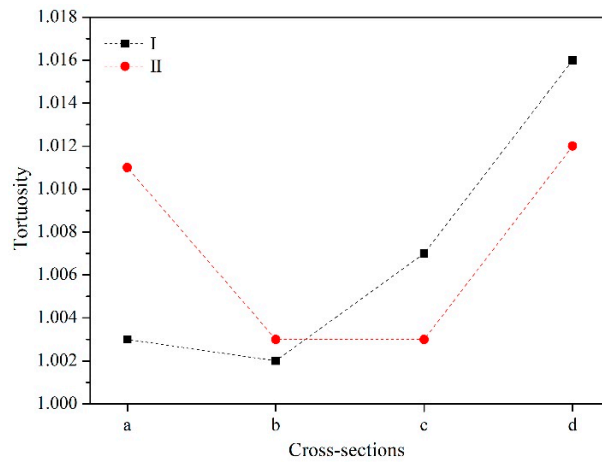


Figure 11. The fractures’ tortuosity in four cross-sections of a 100 mm shale core. The (a), (b), (c), and (d) represent the four cross-sections in Figure 9, while the I and II in the figure are the fracture number in Figure 9.

Furthermore, Figure 12 illustrates the probability distribution of the fracture widths in the 25 mm core. The analysis reveals that the majority of the fracture widths fall within the range of 25 μm to 150 μm , with a maximum value of approximately 250 μm . Notably, the frequency distribution displays the most recurrent values to be within the range of 75 μm to 87 μm .

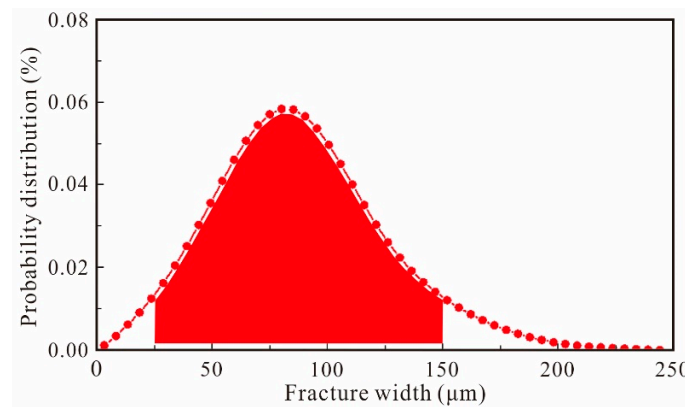


Figure 12. The fracture width probability distribution of the 25 mm core. The red part in the figure shows the main intervals of the fracture width.

4.4. Simulation of Shale Natural Fracture Seepage with Different Sizes

Figure 13a–h presents the simulation results of models obtained from 100 mm and 25 mm shale cores, respectively. Figure 13a,e displays the fracture morphology of the two models. While the fracture in Figure 13e is smaller than in Figure 13a, its morphology is more continuous. The fluid velocity in Figure 13b ranges from 0 to 3 m/s, which is almost 10 times higher than that in Figure 13f, indicating a high degree of permeability. The fracture surface displacement in Figure 13c ranges from 0 to 300 μm , almost three times higher than in Figure 13g. The distribution of fracture surface pressure in Figure 13d,h shows nearly the same pressure range, despite the difference in fracture sizes. Higher pressures only occur at the edge of the fractures in Figure 13d, while they appear throughout the fracture in Figure 13h. The red arrows in Figure 13d,h indicate the direction of fracture surface pressure, which is almost perpendicular to the fracture surface where the fractures bend.

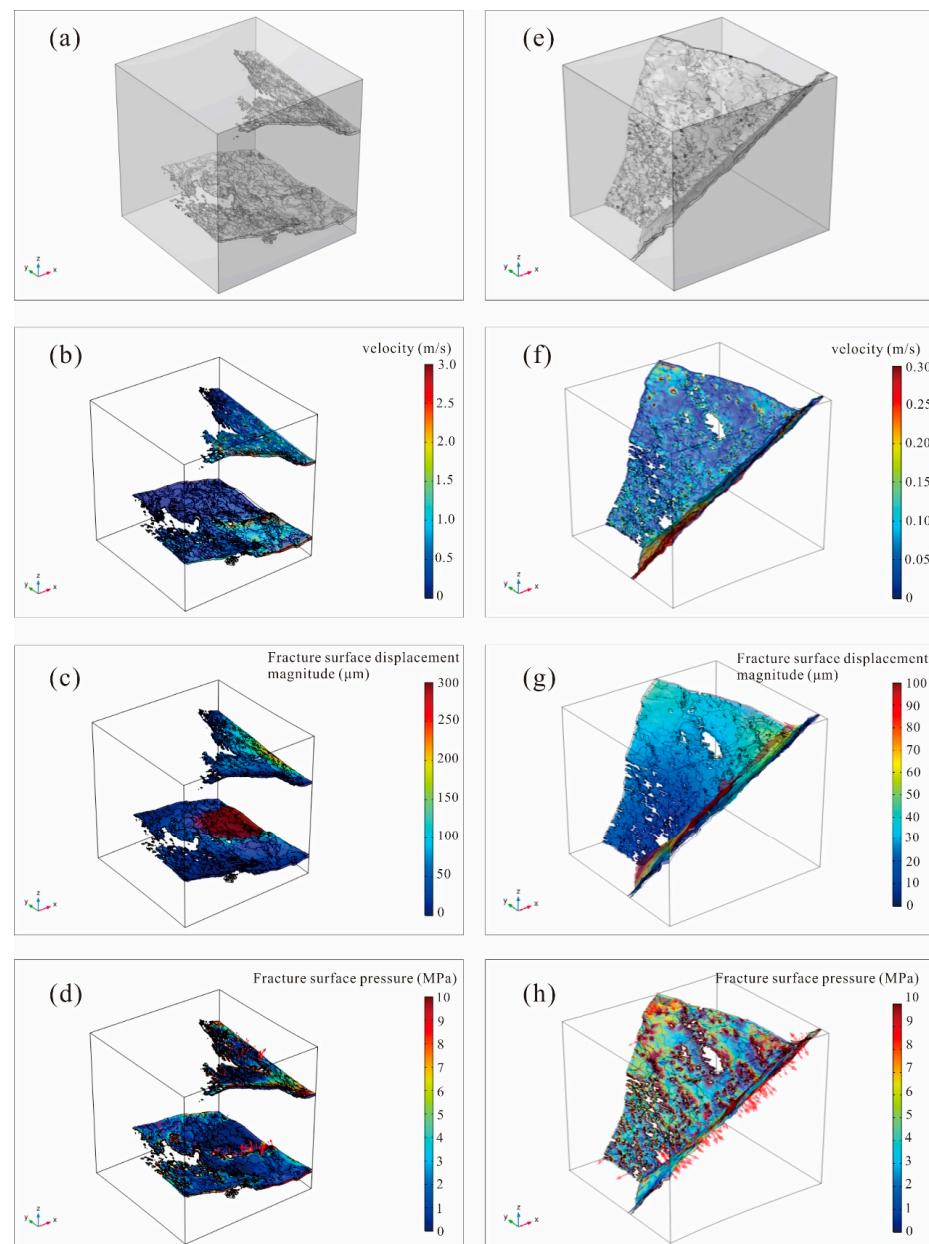


Figure 13. The simulation results show the morphology of fractures (a,e) and the distribution of fluid velocity (b,f), fracture surface displacement (c,g), and fracture surface pressure (d,h) at 10 MPa surrounding pressure.

5. Discussion

5.1. The In Situ Stress Characteristic of the Shale Oil Reservoir

The in situ stress of the target shale reservoir exhibits the characteristic of $\sigma_H > \sigma_v > \sigma_h$, with σ_v and σ_h being particularly similar. The three kinds of stress conditions, including (1) $\sigma_v > \sigma_H > \sigma_h$, (2) $\sigma_H > \sigma_v > \sigma_h$, and (3) $\sigma_H > \sigma_h > \sigma_v$, correspond to normal faulting, strike-slip, and thrust faulting, respectively [58]. This stress pattern tends to result in fracture patterns that follow a strike-slip mechanism (as depicted in Figure 14). The lateral stress coefficient, which represents the ratio of horizontal stresses to vertical stress [59], is a critical parameter for simulating fracture initiation under in situ stress conditions [23]. According to the regression correlation between the lateral stress coefficient and burial depth proposed by Brown and Hoek (1978) [60], the lateral stress coefficient of the target layers should range from 0.333 to 0.998. Nevertheless, the measured value obtained ranged from 1.020 to 1.037, markedly surpassing the theoretically predicted values. A high lateral stress coefficient implies that the horizontal stresses exceed the average level.

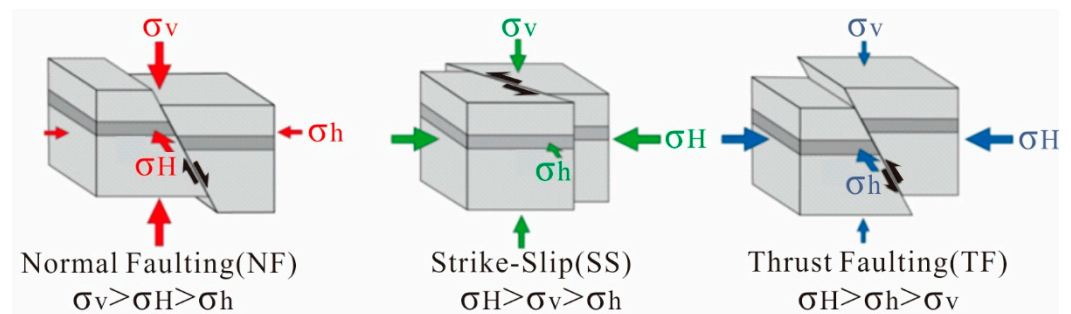


Figure 14. The main tectonic stress patterns. The arrows in the figure demonstrate the direction of the stress, and red, green, and blue colors display different stress patterns.

5.2. Comparison of the Natural Fracture Shale's CT Scanning with Multi-Scales

Three types of shale cores, measuring 100 mm, 25 mm, and 2 mm, were subjected to CT scanning. The 100 mm core revealed fractures with a width at the millimeter level, but due to the low accuracy of the CT scanning, only visible fractures could be detected. Moreover, the pores were almost indiscernible. In contrast, the 25 mm core allowed for a simultaneous display of pores and fractures. Notably, the connecting pores were found to be particularly well-developed near the bedding planes (Figure 6c). Further analysis using the program Avizo revealed that the bedding planes were often discontinuous, and the presence of numerous protrusions significantly increased the volume of fractures. The CT scanning of the 2 mm core yielded a substantially improved resolution, enabling a more comprehensive visualization of the fractures and interconnected pores. However, the higher accuracy of the CT scanning at this scale primarily highlights the pore information, which may not fully capture additional details of the fractures. Thus, in studies focusing on fractures, the 25 mm core size is more appropriate. To summarize, the choice of core size should be guided by the research objectives.

5.3. The Tortuosity Changes in Different Scales

According to Sun et al. (2022) [22] tortuosity is an effective measure of the geometrical complexity of natural fractures. The CT scanning data of the 25 mm shale core indicate that the tortuosity of both long and short fractures exhibited a similar changing trend across different cross-sections. While the tortuosity of an individual long fracture tended to remain stable across different cross-sections, short fractures exhibited more variation in tortuosity, as shown by the data analysis of Figure 15. In particular, the standard deviation of the tortuosity of large fractures was lower than that of small fractures, indicating that the morphology of larger fractures is more likely to remain stable, while small-scale fractures tend to exhibit diverse shapes. Moreover, the standard deviation of tortuosity for large fractures of types I and II from the 100 mm shale core was 0.006 and 0.005, respectively, in

agreement with the data presented in Figure 15. This finding indicates that larger fractures exhibit greater shape stability. Additionally, tortuosity is influenced by frequent changes in the width of a fracture, which are determined by irregularities in the fracture wall.

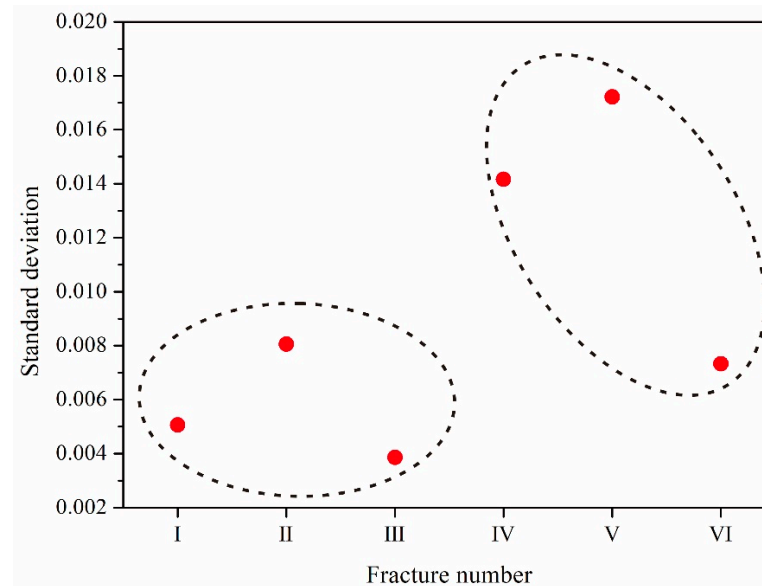


Figure 15. The standard deviation of the fractures of I, II, III, IV, V, and VI. The red dots display the standard deviation of tortuosity, and the dot lines demonstrate the tortuosity of large fractures and small fractures, respectively.

5.4. Sensitivity of Fracture Permeability at Variable Surrounding Pressures

The two fracture models were extracted from the CT results of 100 mm and 25 mm; therefore, the fracture models reflect different sizes at respective scales. The simulation of dynamic fracture permeability response was conducted for shale core sizes of 100 mm and 25 mm while varying the pressure from 2 MPa to 10 MPa, as displayed in Figure 16. The fracture permeability for the 100 mm core varied from $2.04 \times 10^4 \mu\text{m}^2$ to $8.67 \times 10^4 \mu\text{m}^2$, whereas it decreased from $1.3 \times 10^3 \mu\text{m}^2$ to $5.45 \times 10^2 \mu\text{m}^2$ for the 25 mm core. Notably, the fracture permeability of the 100 mm core was almost ten times higher than that of the 25 mm core. Despite the significant difference in fracture size between the two models, as depicted in Figure 13, their permeability exhibited a similar changing trend with varying surrounding pressures. Furthermore, the permeability showed a linear decrease with increasing surrounding pressure, as evidenced by the data, showing a reduction of 2.35 and 2.39 times the initial values for the 100 mm and 25 mm shale cores, respectively. The results indicate that the stress sensitivity of fracture permeability remains consistent across various fracture scales. However, it should be noted that fractures with smaller scales may undergo complete closure when subjected to higher surrounding pressures, leading to the complete loss of permeability. As such, our understanding of fracture behavior relies on the assumption that the fractures do not experience total closure.

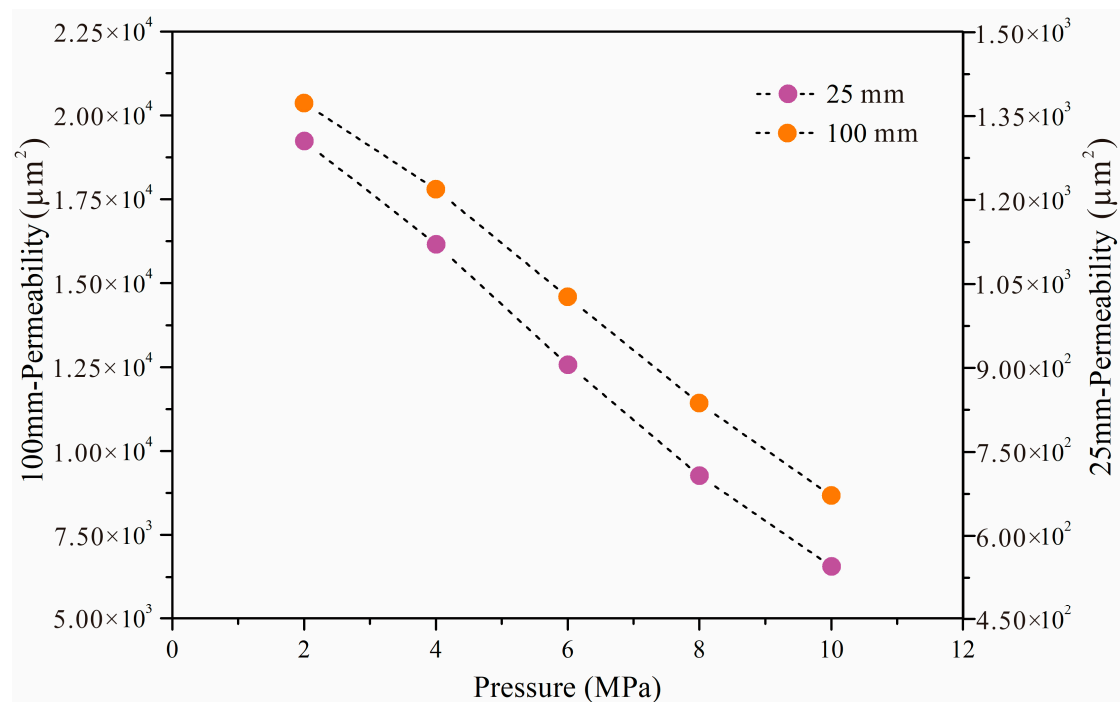


Figure 16. The dynamic permeability changing vs. pressure varies from 2 MPa to 10 MPa. The 100 mm and 25 mm shale cores are simulated.

6. Conclusions

This study utilized a novel and comprehensive approach with the combination of multi-scale CT scanning and numerical simulation of fluid seepage in fracture models to investigate the developmental features of natural fractures in the Lower Jurassic shale oil reservoirs in the Sichuan Basin. The findings of this study can be summarized as follows:

1. The in situ stress of the shale reservoir exhibits the characteristic of $\sigma_H > \sigma_v > \sigma_h$, with σ_v and σ_h being particularly similar, resulting in a strike-slip fracture pattern. The relatively high lateral stress coefficient between 1.020 and 1.037 indicates that the horizontal stresses are higher than the average level. The above understanding helps to predict the natural fracture pattern.
2. While the 2 mm core CT scan offers a more detailed view of the fractures and connected pores, the high-resolution results in more pore information, which may not fully reveal additional information about the fractures. Therefore, if the primary focus of the study is on fractures, then the 25 mm core would be a more suitable option to study the microscopic natural fractures.
3. The tortuosity of various fractures indicates that larger fractures tend to maintain a more stable morphology, whereas smaller-scale fractures tend to exhibit a greater diversity of shapes, which is not conducive to fluid flow.
4. The fracture permeability displays a nearly linear decrease with increasing surrounding pressure, suggesting that the stress sensitivity of fracture permeability is approximately similar across different fracture scales.

Overall, in this research, extensive experimental and numerical simulations are innovatively combined, leading to the comprehensive investigation of microscopic natural fractures in shale oil reservoirs which has significantly improved our understanding of their properties and enabled the identification of favorable areas for shale oil exploration. To advance this research further, we plan to develop numerical fracture models that cater to different natural fracture types in shale oil reservoirs. These models will be integrated with the Thermo-Fluid-Solid coupling method to provide further insights into the evolution mechanism of fracture permeability.

Author Contributions: Conceptualization, S.H.; methodology, S.H., X.B. and X.W.; software, Y.H. and L.C. (Likai Cui); formal analysis, S.H., X.B., W.M., L.C. (Lijuan Cheng) and Z.W.; investigation, S.H., X.B. and Y.W.; resources, S.H., X.B. and W.M.; writing—original draft, S.H. and X.B.; writing—review and editing, S.H., X.B., B.L., M.S. and X.F.; visualization, S.H., X.B. and Y.Z.; supervision, S.H.; funding acquisition, S.H., B.L., M.S. and X.B. All authors have read and agreed to the published version of the manuscript.

Funding: The research work was funded by Heilongjiang Province “Hundred Million” Engineering of Major Projects in Science and Technology (SC2020ZX05A0023) and the Scientific Research and Technological Development Project of China National Petroleum Corporation (2022DJ1809). This study was supported by the National Natural Science Foundation of China (42202155; 42272159; U22A20574), China Postdoctoral Science Foundation (2021MD703807), Heilongjiang Provincial Postdoctoral Science Foundation (LBH-Z20121), China Scholarship Council (202008230018). The authors also acknowledge funding by the Natural Science Foundation of Heilongjiang Province (TD2021D001) and the Key R&D Program of Hainan Province (ZDYF2023GXJS009). The APC was funded by 42202155.

Institutional Review Board Statement: Not applicable.

Informed Consent Statement: Not applicable.

Data Availability Statement: Data are unavailable due to privacy restrictions.

Conflicts of Interest: The authors declare no competing interests.

References

- Fathoni, A.Z.; Batts, B.D. A literature review of fuel stability studies with a particular emphasis on shale oil. *Energy Fuels* **1991**, *5*, 682–693. [[CrossRef](#)]
- Fu, C.Y. China’s shale gas and shale oil resources: Opportunities and challenges. *Energy Explor. Exploit.* **2014**, *32*, 759–769. [[CrossRef](#)]
- Mahzari, P.; Mitchell, T.M.; Jones, A.P.; Oelkers, E.H.; Juri, J.E. Novel laboratory investigation of huff-n-puff gas injection for shale oils under realistic reservoir conditions. *Fuel* **2020**, *285*, 118950. [[CrossRef](#)]
- Liu, B.; Sun, J.; Zhang, Y.; He, J.; Fu, X.; Yang, L.; Xing, J.; Zhao, X. Reservoir space and enrichment model of shale oil in the first member of Cretaceous Qingshankou Formation in the Changling sag, southern Songliao Basin, NE China. *Pet. Explor. Dev.* **2021**, *48*, 608–624. [[CrossRef](#)]
- Wu, T.; Pan, Z.J.; Liu, B.; Connell, L.D.; Fu, X.F. Laboratory characterization of shale oil storage behavior: A comprehensive review. *Energy Fuels* **2021**, *35*, 7305–7318. [[CrossRef](#)]
- Curnow, W.J. The prospects for shale oil in Australia. *Fuel* **1987**, *66*, 292–294. [[CrossRef](#)]
- Zou, C.N.; Yang, Z.; Cui, J.W.; Zhu, R.K.; Hou, L.H.; Tao, S.Z.; Yuan, X.J.; Wu, S.T.; Lin, S.H.; Wang, L.; et al. Formation mechanism, geological characteristics and development strategy of nonmarine shale oil in China. *Pet. Explor. Dev.* **2013**, *40*, 5–27. [[CrossRef](#)]
- Solarin, S.A.; Gil-Alana, L.A.; Lafuente, C. An investigation of long range reliance on shale oil and shale gas production in the U.S. market. *Energy* **2020**, *195*, 116933. [[CrossRef](#)]
- Liu, B.; Yang, Y.; Li, J.; Chi, Y.; Li, J.; Fu, X. Stress sensitivity of tight reservoirs and its effect on oil saturation: A case study of Lower Cretaceous tight clastic reservoirs in the Hailar Basin, Northeast China. *J. Pet. Sci. Eng.* **2020**, *184*, 106484. [[CrossRef](#)]
- Liu, B.; Wang, Y.; Tian, S.; Guo, Y.; Wang, L.; Yasin, Q.; Yang, J. Impact of thermal maturity on the diagenesis and porosity of lacustrine oil-prone shales: Insights from natural shale samples with thermal maturation in the oil generation window. *Int. J. Coal Geol.* **2022**, *261*, 104079. [[CrossRef](#)]
- Bai, L.H.; Liu, B.; Du, Y.J.; Wang, B.Y.; Tian, S.S.; Wang, L.; Xue, Z.Q. Distribution characteristics and oil mobility thresholds in lacustrine shale reservoir: Insights from N₂ adsorption experiments on samples prior to and following hydrocarbon extraction. *Pet. Sci.* **2022**, *19*, 486–497. [[CrossRef](#)]
- Cui, D.; Yin, H.L.; Liu, Y.P.; Li, J.; Pan, S.; Wang, Q. Effect of final pyrolysis temperature on the composition and structure of shale oil: Synergistic use of multiple analysis and testing methods. *Energy* **2022**, *252*, 124062. [[CrossRef](#)]
- Orangi, A.; Nagarajan, N.R.; Honarpour, M.M.; Rosenzweig, J. Unconventional shale oil and gas-condensate reservoir production, impact of rock, fluid, and hydraulic fractures. In Proceedings of the SPE Hydraulic Fracturing Technology Conference, The Woodlands, TX, USA, 24–26 January 2011. [[CrossRef](#)]
- Boak, J.; Kleinberg, R. 4–Shale Gas, Tight Oil, Shale Oil and Hydraulic Fracturing. In *Future Energy*, 3rd ed.; Elsevier: Amsterdam, The Netherlands, 2020; pp. 67–95.
- Shaldybin, M.V.; Wilson, M.J.; Wilson, L.; Lopushnyak, Y.M.; Brydson, R.; Krupskaya, V.V.; Kondrashova (Deeva), E.S.; Glotov, A.V.; Goncharov, I.V.; Samoilenko, V.V.; et al. The nature, origin and significance of luminescent layers in the Bazhenov Shale Formation of West Siberia, Russia. *Mar. Pet. Geol.* **2019**, *100*, 358–375. [[CrossRef](#)]
- Khakimova, L.; Bondarenko, T.; Cheremisin, A.; Myasnikov, A.; Varfolomeev, M. High pressure air injection kinetic model for Bazhenov Shale Formation based on a set of oxidation studies. *J. Pet. Sci. Eng.* **2019**, *172*, 1120–1132. [[CrossRef](#)]

17. Mukhina, E.; Cheremisin, A.; Khakimova, L.; Garipova, A.; Dvoretzkaya, E.; Zvada, M.; Kalacheva, D.; Prochukhan, K.; Kasyanenko, A.; Cheremisin, A. Enhanced oil recovery method selection for shale oil based on numerical simulations. *ACS Omega* **2021**, *6*, 23731–23741. [[CrossRef](#)]
18. Zou, C.N.; Pan, S.Q.; Jing, Z.H.; Gao, J.L.; Yang, Z.; Wu, S.T.; Zhao, Q. Shale oil and gas revolution and its impact. *Acta Pet. Sin.* **2020**, *41*, 1–12.
19. Jin, Z.J.; Liang, X.P.; Bai, Z.R. Exploration breakthrough and its significance of Gulong lacustrine shale oil in the Songliao Basin, Northeastern China. *Energy Geosci.* **2022**, *3*, 120–125. [[CrossRef](#)]
20. Wang, X.; He, S.; Guo, X.W.; Zhang, B.Q.; Chen, X.H. The Resource Evaluation of Jurassic Shale in North Fuling Area, Eastern Sichuan Basin, China. *Energy Fuels* **2018**, *32*, 1213–1222. [[CrossRef](#)]
21. Gale, J.F.W.; Laubach, S.E.; Olson, J.E.; Eichhülle, P.; Fall, A. Natural fractures in shale: A review and new observations. *AAPG Bull.* **2014**, *98*, 2165–2216. [[CrossRef](#)]
22. Sun, S.S.; Huang, S.P.; Gomez-Rivas, E.; Griera, A.; Liu, B.; Xu, L.L.; Wen, Y.R.; Dong, D.Z.; Shi, Z.S.; Chang, Y.; et al. Characterization of natural fractures in deep-marine shales: A case study of the Wufeng and Longmaxi shale in the Luzhou Block Sichuan Basin, China. *Front. Earth Sci.* **2022**, 1–14. [[CrossRef](#)]
23. Huang, S.P.; Liu, D.M.; Yao, Y.B.; Gan, Q.; Cai, Y.D.; Xu, L.L. Natural fractures initiation and fracture type prediction in coal reservoir under different in-situ stresses during hydraulic fracturing. *J. Nat. Gas Sci. Eng.* **2017**, *43*, 69–80. [[CrossRef](#)]
24. Zhou, J.; Zhang, L.Q.; Li, X.; Pan, Z.J. Experimental and modeling study of the stress-dependent permeability of a single fracture in shale under high effective stress. *Fuel* **2019**, *257*, 116078. [[CrossRef](#)]
25. Huang, S.P.; Liu, D.M.; Cai, Y.D.; Gan, Q. In-situ stress distribution and its impact on CBM reservoir properties in the Zhengzhuang area, southern Qinshui Basin, North China. *J. Nat. Gas Sci. Eng.* **2019**, *61*, 83–96. [[CrossRef](#)]
26. Sun, M.D.; Wen, J.J.; Pan, Z.J.; Liu, B.; Blach, T.P.; Ji, Y.P.; Hu, Q.H.; Yu, B.S.; Wu, C.M.; Ke, Y.B. Pore accessibility by wettable fluids in overmature marine shales of China: Investigations from contrast-matching small-angle neutron scattering (CM-SANS). *Int. J. Coal Geol.* **2022**, *255*, 103987. [[CrossRef](#)]
27. Hazra, B.; Vishal, V.; Sethi, C.; Chandra, D. Impact of supercritical CO₂ on shale reservoirs and its implication for CO₂ sequestration. *Energy Fuels* **2022**, *36*, 9882–9903. [[CrossRef](#)]
28. Jia, B.; Tsau, J.; Barati, R. A review of the current progress of CO₂ injection EOR and carbon storage in shale oil reservoirs. *Fuel* **2019**, *236*, 404–427. [[CrossRef](#)]
29. Elenius, M.; Skurtveit, E.; Yarushina, V.; Baig, I.; Sundal, A.; Wangen, M.; Landschulze, K.; Kaufmann, R.; Choi, J.C.; Hellevang, H.; et al. Assessment of CO₂ storage capacity based on sparse data: Skade Formation. *Int. J. Greenh. Gas Control* **2018**, *79*, 252–271. [[CrossRef](#)]
30. van Noort, R.; Yarushina, V. Water, CO₂ and argon permeabilities of intact and fractured shale cores under stress. *Rock Mech. Rock Eng.* **2019**, *52*, 299–319. [[CrossRef](#)]
31. Peshkov, G.A.; Khakimova, L.A.; Grishko, E.V.; Wangen, M.; Yarushina, V.M. Coupled basin and hydro-mechanical modeling of gas chimney formation: The SW Barents Sea. *Energies* **2021**, *14*, 6345. [[CrossRef](#)]
32. Yarushina, V.M.; Wang, L.H.; Connolly, D.; Kocsis, G.; Fæstø, I.; Polteau, S.; Lakhlifi, A. Focused fluid-flow structures potentially caused by solitary porosity waves. *Geology* **2022**, *50*, 179–183. [[CrossRef](#)]
33. Gale, J.F.W.; Reed, R.M.; Holder, J. Natural fractures in the Barnett Shale and their importance for hydraulic fracture treatments. *AAPG Bull.* **2007**, *91*, 603–622. [[CrossRef](#)]
34. Wei, Y.; Hu, X.; Liu, M.; Wang, W. Investigation of the effect of natural fractures on multiple shale-gas well performance using non-intrusive EDFM technology. *Energies* **2019**, *12*, 932.
35. Pirzada, M.A.; Bahaaddini, M.; Moradian, O.; Roshan, H. Evolution of contact area and aperture during the shearing process of natural rock fractures. *Eng. Geol.* **2021**, *291*, 106236. [[CrossRef](#)]
36. Zhang, C.; Liu, D.D.; Jiang, Z.X.; Song, Y.; Luo, Q.; Wang, X. Mechanism for the formation of natural fractures and their effects on shale oil accumulation in Junggar Basin, NW China. *Int. J. Coal Geol.* **2022**, *254*, 103973. [[CrossRef](#)]
37. Xian, C.; Zhang, J.; Zhao, C.; Wang, G.; Xing, L. Characterizing and modeling multi-scale natural fractures in the Ordovician-Silurian Wufeng-Longmaxi Shale Formation in South Sichuan Basin. In Proceedings of the Unconventional Resources Technology Conference, Austin, TX, USA, 24–26 July 2017.
38. Micheal, M.; Xu, W.L.; Xu, H.Y.; Zhang, J.N.; Jin, H.J.; Yu, H.; Wu, H.A. Multi-scale modelling of gas transport and production evaluation in shale reservoir considering crisscrossing fractures. *J. Nat. Gas Sci. Eng.* **2021**, *95*, 104156. [[CrossRef](#)]
39. Volatili, T.; Agosta, F.; Cardozo, N.; Zambrano, M.; Lecomte, I.; Tondi, E. Outcrop-scale fracture analysis and seismic modelling of a basin-bounding normal fault in platform carbonates, central Italy. *J. Struct. Geol.* **2022**, *155*, 104515. [[CrossRef](#)]
40. Laubach, S.E.; Olson, J.E.; Gale, J.F.W. Are open fractures necessarily aligned with maximum horizontal stress? *Earth Planet. Sci. Lett.* **2004**, *222*, 191–195. [[CrossRef](#)]
41. Rajabi, M.; Sherkati, S.; Bohlooli, B.; Tingay, M. Subsurface fracture analysis and determination of in-situ stress direction using FMI logs: An example from the Santonian carbonates (Ilam Formation) in the Abadan Plain, Iran. *Tectonophysics* **2010**, *492*, 192–200. [[CrossRef](#)]
42. Zhang, Y.Y.; He, Z.L.; Jiang, S.; Lu, S.F.; Xiao, D.S.; Chen, G.H.; Li, Y.C. Fracture types in the lower Cambrian shale and their effect on shale gas accumulation, Upper Yangtze. *Mar. Pet. Geol.* **2019**, *99*, 282–291. [[CrossRef](#)]

43. Zhang, X.; Lu, Y.; Tang, J.; Zhou, Z.; Liao, Y. Experimental study on fracture initiation and propagation in shale using supercritical carbon dioxide fracturing. *Fuel* **2016**, *190*, 370–378. [[CrossRef](#)]
44. Wu, S.T.; Zhai, X.F.; Yang, Z.; Bale, H.; Hong, Y.L.; Cui, J.W.; Pan, S.Q.; Lin, S.H. Characterization of fracture formation in organic-rich shales—An experimental and real time study of the Permian Lucaogou Formation, Junggar Basin, northwestern China. *Mar. Pet. Geol.* **2019**, *107*, 397–406. [[CrossRef](#)]
45. Gou, Q.; Xu, S.; Hao, F.; Yang, F.; Zhang, B.; Shu, Z.; Zhang, A.; Wang, Y.; Lu, Y.; Cheng, X.; et al. Full-scale pores and micro-fractures characterization using FE-SEM, gas adsorption, nano-CT and micro-CT: A case study of the Silurian Longmaxi Formation shale in the Fuling area, Sichuan Basin, China. *Fuel* **2019**, *253*, 167–179. [[CrossRef](#)]
46. Chen, Y.; Jiang, C.; Leung, J.Y.; Wojtanowicz, A.K.; Zhang, D. Multiscale characterization of shale pore-fracture system: Geological controls on gas transport and pore size classification in shale reservoirs. *J. Pet. Sci. Eng.* **2021**, *202*, 108442. [[CrossRef](#)]
47. Sun, M.D.; Yu, B.S.; Hu, Q.H.; Chen, S.; Xia, W.; Ye, R.C. Nanoscale pore characteristics of the Lower Cambrian Niutitang Formation Shale: A case study from Well Yuke #1 in the Southeast of Chongqing, China. *Int. J. Coal Geol.* **2016**, *154–155*, 16–29.
48. Sun, M.D.; Zhang, L.H.; Hu, Q.H.; Pan, Z.J.; Yu, B.S.; Sun, L.W.; Bai, L.F.; Fu, H.J.; Zhang, Y.F.; Zhang, C.; et al. Multiscale connectivity characterization of marine shales in southern China by fluid intrusion, small-angle neutron scattering (SANS), and FIB-SEM. *Mar. Pet. Geol.* **2020**, *112*, 104101. [[CrossRef](#)]
49. Tan, Y.; Pan, Z.; Liu, J.; Wu, Y.; Haque, A.; Connell, L.D. Experimental study of permeability and its anisotropy for shale fracture supported with proppant. *J. Nat. Gas Sci. Eng.* **2017**, *44*, 250–264. [[CrossRef](#)]
50. Bird, M.B.; Butler, S.L.; Hawkes, C.D.; Kotzer, T. Numerical modeling of fluid and electrical currents through geometries based on synchrotron X-ray tomographic images of reservoir rocks using Avizo and COMSOL. *Comput. Geosci.* **2014**, *73*, 6–16. [[CrossRef](#)]
51. He, W.Y.; Bai, X.F.; Meng, Q.A.; Li, J.H.; Zhang, D.Z.; Wang, Y.Z. Accumulation geological characteristics and major discoveries of lacustrine shale oil in Sichuan Basin. *Acta Pet. Sin.* **2022**, *43*, 885–898.
52. Erarslan, N.; Liang, Z.Z.; Williams, D.J. Experimental and numerical studies on determination of indirect tensile strength of rocks. *Rock Mech. Rock Eng.* **2012**, *45*, 739–751. [[CrossRef](#)]
53. Dutler, N.; Nejati, M.; Valley, B.; Amann, F.; Molinari, G. On the link between fracture toughness, tensile strength, and fracture process zone in anisotropic rocks. *Eng. Fract. Mech.* **2018**, *201*, 56–79. [[CrossRef](#)]
54. Kaiser, J. Erkenntnisse und Folgerungen aus der Messung von Geräuschen bei Zugbeanspruchung von metallischen Werkstoffen. *Arch. Eisenhüttenwesen* **1953**, *24*, 43–45. [[CrossRef](#)]
55. Lehtonen, A.; Cosgrove, J.W.; Hudson, J.A.; Johansson, E. An examination of in situ rock stress estimation using the Kaiser effect. *Eng. Geol.* **2012**, *124*, 24–37. [[CrossRef](#)]
56. Hou, Y.D.; Huang, S.P.; Han, J.; Liu, X.B.; Han, L.F.; Fu, C.F. Numerical simulation of the effect of injected CO₂ temperature and pressure on CO₂-Enhanced coalbed methane. *Appl. Sci.* **2020**, *10*, 1385.
57. Espino, D.M.; Shepherd, D.E.T.; Hukins, D.W.L. Transient large strain contact modelling: A comparison of contact techniques for simultaneous fluid–structure interaction. *Eur. J. Mech. B-Fluids* **2015**, *51*, 54–60. [[CrossRef](#)]
58. Heidbach, O.; Rajabi, M.; Cui, X.; Fuchs, K.; Müller, B.; Reinecker, J.; Reiter, K.; Tingay, M.; Wenzel, F.; Xie, F.; et al. The World Stress Map database release 2016: Crustal stress pattern across scales. *Tectonophysics* **2018**, *744*, 484–498. [[CrossRef](#)]
59. Hoek, E.; Brown, E.T. *Underground Excavation in Rock*; CRC Press: Boca Raton, FL, USA, 1980.
60. Brown, E.T.; Hoek, E. Trends in relationships between measured in-situ stresses and depth. *Int. J. Rock Mech. Min. Geomech. Abstr.* **1978**, *15*, 211–215. [[CrossRef](#)]

Disclaimer/Publisher’s Note: The statements, opinions and data contained in all publications are solely those of the individual author(s) and contributor(s) and not of MDPI and/or the editor(s). MDPI and/or the editor(s) disclaim responsibility for any injury to people or property resulting from any ideas, methods, instructions or products referred to in the content.